SPE 124690

Numerical Simulation of Seismicity Induced by Hydraulic Fracturing in Naturally Fractured Reservoirs

X.P. Zhao, SPE, and R.P. Young, University of Toronto

This paper was prepared for presentation at the 2009 SPE Annual Technical Conference and Exhibition held in New Orleans, Louisiana, USA, 4–7 October 2009.

Abstract

The problem of the interaction between hydraulic and natural fractures is of great interest for energy resource industry because natural fractures can significantly influence the overall geometry and effectiveness of hydraulic fractures. Based on the tri-axial fracturing lab experiments presented in other publications and fluid stimulation in the field, a 2D discrete element model with fully dynamic and hydromechanical coupling is validated to simulate fluid injection into a reservoir containing a natural fracture by comparing modeling geometries of hydraulic fractures and induced seismicity with actual results in laboratory and field data.

At the lab scale, the numerical model simulated a series of fracturing experiments on rock blocks with pre-fractures with different orientation, and the model captured three interaction types (crossing, dilating, and arresting) between induced fractures and pre-fractures and also illustrated three types of crossing depending on the differential stresses and orientations of pre-fractures. Furthermore, seismic mechanisms obtained from the model confirmed that hydraulic fractures were arrested by shear slippage of the pre-fracture. In the field scale, the calibrated model simulated the stimulation conducted in the tight gas reservoir at Dowdy Ranch field, USA. The model produced the scope and orientation of induced fractures similar to results obtained from the actual recorded microseismicity, and a similar seismic magnitude range. Moreover, the model showed deformation and cracking occurring ahead of the fluid pressure front and hydraulic fractures were arrested by the dilation of the fault. At the same time, the leakage of large fluid volume through the fault area was qualitatively prediected by the 2D model. These confirmed that the effective half-length is shorter than the created fracture half-length deduced from microseismic locations, which is the case during the multistage fracturing treatment in the Bossier formation. In addition, from the modeling results, it was concluded that the horizontal principal stresses with a ratio no less than 2 may be enough to cross a natural fracture with a single hydraulic fracture. Therefore, the validated model can help examine in detail the micromechanism behind the failure, and the relationship between the induced seismicity and the fluid front through direct observation of the model.

Introduction

Hydraulic fracturing and seismic monitoring are established techniques to improve the production of hydrocarbons from unconventional oil and gas reservoirs (Pearson 1981; Maxwell and Urbancic 2001; Sharma et al. 2004; Le Calvez et al. 2006), enhance geothermal energy in hot dry rock (Sasaki 1998; Norio et al. 2008), and facilitate slurry waste re-injection operations(Warpinski et al. 1999). Due to ubiquitous natural fractures, the problem of the interaction between hydraulic and natural fractures is of great interest for the energy resource industry because natural fractures can significantly influence the overall geometry and effectiveness of hydraulic fractures.

A considerable amount of research has been carried out in the past few decades trying to understand the complexity and mechanics of hydraulic fractures in fractured reservoirs. Blanton (1986) conducted scaled laboratory experiments on naturally fractured Devonian shale and hydrostone under different angles of approach and states of stress. These experiments shew that hydraulic fractures crossed pre-fractures only under high differential stress and high approaching angles, while at low differential stress and angles of approach the existing fracture opened, diverting the fracturing fluid and preventing the induced fracture from crossing, at least temporarily. Beugelsdijk et al. (2000) also performed laboratory experiments on Portland cement blocks to analyze complex hydraulic fracture geometry as a function of horizontal stress difference, stress regime, flow rate and discontinuity pattern. Many field work took in naturally fractured formations reveal that effects of natural fractures on fracture propagation are enhanced fluid leakoff, premature screenout, arrest of the fracture propagation, formation of multiple fracures, fracture offsets, high net pressures (Britt and Hager 1994; Vinod et al. 1997; Rodgerson 2000; Azeemuddin et al. 2002; Sharma et al. 2004).

Regarding the mechanics of hydraulic fracture, Murphy and Fehler (1986) carried out some numerical work based on reservoir stimulation experiments in Hot Dry Rock. They demonstrated that branching or dendritic fractures were resulted from the shear slippage along the pre-existing joints in the rock. Renshaw and Pollard (1995) provided a simple criterion for crossing. According to this work, compressinal crossing will occur if the magnitude of the compression acting perpendicular to the frictional interface is sufficient to prevent slip along the interface at the moment when the stress ahead of the fracture tip is sufficient to initiate a fracture on the opposite side of the interface. Zhou et al. (2008) conducted a series of servo-controlled tri-axial fracturing experiments on cement sand blocks to clarify the mechanism of hydraulic fractures interaction with a pre-existing fracture with shear strength while comparing with the geometry of hydraulic fractures. They found that crossing/dilating is dominating fracture behavior for natural fracture with a small/larger aperture, respectively.

Microseismic locations can delineate the extent of fracturing and seismic source mechanisms can yield information about the nature of deformation. In hydraulic fracturing, microseismic events often have clear S-waves but their P-waves are small and difficult to be accurately picked (Murphy and Fehler 1986; Fischer et al. 2008). In addition, source mechanisms from microseismic data usually indicate that predominant mode of deformation is shearing on preexisting joints (Sasaki and Kaieda 2002). However, traditional modeling methods generally use a fracture mechanics approach to calculate fracture growth and assume that new fractures are growing in tension parallel to the maximum stress (Economides and Nolte 1989; Dong and de Pater 2001; Adachi et al. 2007; Akulich and Zvyagin 2008). For this reason, some attempts have been made by use of the distinct element method (DEM) in which the rock is divided into deformable blocks or particles with fluid flowing between them (Pine and Cundall 1985; Jing et al. 2001; Zhang and Sanderson 1996). These models have met with some success but the possible fracture geometries are generally limited and there is no possibility of new fracture formation. Hazzard et al. (2002b) developed a discontinuum method to model the fluid injection in a Hot Dry rock reservoir. They produced realistic fluid pressure histories, realistic seismic source parameters, and asymmetrical growth of hydrofractures, but they did not include realistic joint geometries but random network of joints, and also did not consider the mechanical changes in domain volumes causing changes in domain pressures. Moreover, there is much that still can not be revealed by the microseismic data including the relationship between the fluid front and induced fracture, and the location and nature of any aseismic deformation, what’s more, the effect of natural fracture on the propagation of an induced hydraulic fracture is still not fully understood.

In this paper, a fully dynamic 2D distinct element model was validated to simulate fluid injection into a reservoir containing a natural fracture by comparing modeling geometries of hydraulic fractures or/and induced seismicity with actual results in laboratory experiments presented in other publications and fluid stimulation in a tight gas sand at Dowdy Ranch field, USA. The model enables us to examine in detail the interaction between fluid pressure, rock deformation and slip on existing fractures. The validated numerical models can help elucidate our understanding the mechanics behind the seismicity, and could possibly deliver extra information such as areas where aseismic deformation might be occurring and the relationship between the seismicity, stress/damage and the fluid front.

Modeling Method

The particle flow code (PFC^{2D}) is a tow-dimentional distinct element geomechanical modeling program in which the rock material is modeled as an assembly of round particles (disks) jointed together with breakable bonds with specific strength at contact points. Under the applied load, the bonds can break and a small crack can form. By further generation of these microcracks, a fracture can develop from the linking of individual microcracks. The micro-stiffness and micro-strength of particles can be adjusted to reproduce realistic macro-rock behavior. PFC has been applied to study mechanical behavior of sandstones, granites and other rocks under different stress conditions with much success, such as thermally fracturing experiments (Wanne and Young 2008), hydraulic fracturing (Al-Busaidi et al. 2005), seismic velocities (Hazzard and Young 2004b), core mechanics (Holt et al. 2000), in-situ failure tests (Potyondy and Autio 2001), and large-scale underground excavations (Cai et al. 2007). A thorough description of the PFC model for rocks was given by Potyondy and Cundall (2004).

PFC uses an explicit approach to solve the equation of motion. This allows a dynamic simulation in which seismic waves propagate out from new faults and fractures. Each bond breakage is assumed to be a microcrack. The crack location is assumed to be the contact between the two particles, and the orientation of the crack is assumed to be perpendicular to the line joining the two centers. When a bond breaks, part of stored strain energy is released in the form of a seismic wave. Microcracks occuring close in both space and time are considered a single seismic event if the models are run dynamically by specifying low levels of numerical damping that simulates realistic levels of attenuation in the rock (Hazzard and Young 2000 and 2004a). Seismic source information can therefore be calculated for seismicity. A numerical modeling technique to link the mechanics of fracture formation and the resulting seismicity was described by Hazzard and Young (2002a). This technique calculates the moment tensor (source mechanism) for each event by summing the different components of moment at the contacts surrounding the source. The moment magnitude is then computed from elements of the moment tensor matrix (Feignier and Young 1992).

A technique for simulating fluid flow in PFC is adapted from the algorithm by Cundall (2000). Cundall’s fluid flow is simulated by assuming that each particle contact is a flow channel (pipe) and that these channels connect up small “reservoirs” that store some fluid pressure. As shown in **Fig. 1**, the fluid network topology is generated by drawing lines between the centers of all particles in contact. This creates a series of enclosed domains. The center of each of these domains is stored as a “reservoir”. The reservoirs are then connected by pipes. One pipe exists for each particle contact. Therefore, each reservoir is surrounded completely by contacts and has some volume associated with it. For a 2D model, fluid flow through a pipe is approximated by laminar flow through parallel plates with some aperture associated with it. The rate of volumetric flow can be given by

$$Q = (w^3 \Delta P) \big/ (12 \mu L) \,, \tag{1}$$

where w is the aperture, ΔP is the pressure difference between the two adjacent domains, μ is the fluid viscosity, and L is the length of the pipe (Bear 1972; Al-Busaidi et al. 2005). Because the model is in 2D, an out of plane thichness of 1 is assumed and L is taken to be the distance between the centers of the adjacent domains in question.

Fluid pressures stored in the domains are updated during the fluid calculation, and act on the surrounding particles as equivalent body forces. The change in fluid pressure (ΔP) within each domain, resulting from the flow from the surrounding pipes ($\sum Q$) in one time step (Δt) can then be calculated from the fluid bulk modulus (K_f) and the apparent volume of the domain (ΔV_d) by application of the continuity equation in the form (Al-Busaidi et al. 2005)

$$\Delta P = \frac{K_f}{V_d} (\sum Q \Delta t - \Delta V_d) \ . \tag{2}$$

Hazzard et al. (2002b) and Al-Busaidi et al. (2005) considered the mechanical term (ΔV_d) negligible and did not include it in the calculation of domain pressure changes. However, in the paper we take full equation (2) because the pressure variation caused by domain volumetric change may be significant especially for the areas with induced and natural fractures.

For particles that are just touching (with 0 normal force) a residual aperture, w_0 is assumed. So fluid can still pass through a model with no cracks. When the compressive normal force at a contact increases, the aperture is simply related to the force by

$$w = w_0 F_0 \big/ (F + F_0) \,, \tag{3}$$

where F is the compressive normal force at the contact and F_0 is the normal force at which the pipe aperture decreases to $w_0/2$. The fluid exerts a force on the surrounding particles proportional to the pressure in the domain. This means that the fully hydromechanical coupling exists because a change in mechanical normal force at a contact will alter the pipe aperture and affect the rate of flow, and similarly a change in fluid pressure is capable of moving particles and causing deformation.

The macropermeability of the model can be determined in terms of microparameters. In the case of an isotropic medium, the Darcy flow rate (unit of velocity) is given by

$$q = \frac{k \Delta P}{\mu L} \,, \tag{4}$$

where k is the permeability. The flow rate can also be given by the volume average of flow contibutions of all pipes within a control volume (V)

$$q = \frac{1}{V} \sum_{pipes} q_p V_p \ (q_p = Q / A), \tag{5}$$

where q_p is the flow in a pipe, V_p is the volume of a pipe, A is the pipe cross-sectional area assuming a thickness of 1, and the summation is over all pipes in volume, V. So from equations (1), (4), and (5), the scalar macropermeability, k, can be expressed by

$$k = \frac{1}{12V} \sum_{pipes} L w^3 \,, \tag{6}$$

If we assume that all apertures are the same (this is valid only for a statistically uniform assembly), the aperture can be calculated by

$$w_0 = \sqrt[3]{12kV \big/ (\sum_{pipes} L)} \,, \tag{7}$$

In this way, the residual aperture required for a given permeability (k) can be estimated. This assumes that each contact is just toughing and the normal force is exactly zero. To assess the accuray of this estimation, the permeability can be calculated from equation (6) and the aperture of each contact can be calculated by use of equation (3) (with the value of w calculated in equation (7) used for w_0 in equation (3)). In general the permeability calculated in this way will be less than the set permeability because most of the contacts will be experiencing compression; therefore the apertues will be smaller than the estimated residual aperture and the stress-dependent permeability can be realized for pipes in the model. In addition, we adopted the main modification by Hazzard et al. (2002b) who considered that for the “open” fractures (where the particles are not in contact), the fracture permeability is assumed to be infinite and the reservoir pressures on either side of the channel are set to a weighted average of the two pressures.

Furthermore, to mimic the natural fractures in the model, the bonds are weakened compared with their intact strength within the range of the pre-fracture and the strength ratio is denoted by α, at the same time, among the pre-fracture the residual apertures of their pipes are increased according to equations (1) and (4) and the residual aperture ratio is denoted by β. For example, the residual apertures within a natural fracture become 2 times that in the rest of pipes if the permeability of the natural fracture is 8 times higher.

Model Validation by Laboratory Experimental Data

Zhou et al. (2008) conducted a series of servo-controlled tri-axial fracturing experiments to study the hydraulic fracture propagation behavior and fracture geometry in naturally fractured cubic cement-sand blocks of 300mm. **Fig. 2** shows the schematic plan view of hydraulic fracture intersecting pre-fracture for the laboratory experiments. The openhole section in the center is applied the fluid pressure. Along the direction of hydraulic fracute propagation in far field, parallel to the direction of maximum horizontal stress σ_1 (σ_3 is the minimum horizontal stress), a single closed natural fracture intersects with hydraulic fracture with an angle of approach θ. According to the Mohr-Coulomb criteria (Jaege el al. 2007), shear slippage occurs if the shear stress (τ) resulted from the normal stress (σ_n) and pore pressure acting on the plane of the natural fracutes is higher than the shear stress encountering the Coulomb-Mohr failure envelope. Zhou et al. (2008) used three types of paper (rice paper, printer paper and wrapping paper) with different thickness prescribed into blocks to simulate natural fractures. The coefficient and cohesion of the pre-fracture were obtained from the direct shear tests, which can be used to estimate the shear strength of pre-fracture and compare with the unconfined compressive strength of the sample to find the ratio, α. After hydraulic fracturing tests, they observed three interaction types (cross, dilate, and arrest) between induced fractures with pre-fracture depending on the difference of horizontal stress, angle of approach (θ) and shear strength of pre-fracture. Here, we use the DEM mentioned above to model the fluid stimulation in the second type of pre-fracture (i.e., printer paper).

Table 1 list the basic parameters used to hydraulic fracturing models referring to the actual laboratory values. For the simplicity, the symbols in Table 1, r, r_g, ϕ, L_d, L_h, L_t, E, ν, σ_c, σ_t, and q_i are average grain radius of sample, grain size ratio (maximum/minimum), porosity of sample, the distance between the wellbore and the center of pre-fracture, half-length of pre-fracture, thickness of pre-fracture, Young's modulus, Poisson's ratio, unconfined compressive strength, tensile strength, and fluid injection rate, respectively. Firstly, a compacted and bonded assembly of particles was calibrated by varying its micro-properties to match the corresponding macro-properties of the sample by use of the routine described by Potyondy and Cundall (2004). Table 1 also lists the model calibration results, which indicates that the macro-properties (E, ν, and σ_c) are well reproduced by the PFC^{2D} model. To reduce the calculation cost, the grain of the current model does not represent an actual grain size and totally there are 27,379 bonded particles composing the 300mm×300mm sample. Also, the porosity of the model appears be much larger than the lab value because it was calculated only by the sample volume subtracting the occupied volume by all particles, and if the volume of cements between particles was substracted, the porosity of the model should be much smaller. Furthermore, the macropermeability of the model is less than the specified permeability because many of the pipes are closing under compression. We assumed that the permeability of pipes in the pre-fracture was eight times that in the rest of pipes (i.e., β=2). In addition, the injection rate in the PFC model can not be easily related to the actual injection rate because of the 2D nature of the model, so a rate was chosen that was fast enough to induce fracturing and result in reasonable model run times, but slow enough to maintain stability.

For a series of hydraulic fracturing experiments on blocks with the printer paper as the pre-fracture, Zhou et al. (2008) tested three interaction angles ($\theta = 30^\circ, 60^\circ$, and 90°) and four combinations of confining stresses (σ_1-σ_3=13-3, 10-3, 10-5, and 8-5, i.e., the differential stress $\Delta\sigma$=10MPa, 7MPa, 5MPa, and 3MPa). Three types of interactions between hydraulic fractures and pre-fracures were observed in these tests. Zhou et al. (2008) found that hydraulic fractures crossed the pre-fracture, were arrested by opening and dilating the pre-fracture as indicated by fluid flow along the pre-fracture, and were arrested by shear slippage of the pre-fracture with no dilation and fluid flow along the pre-fracture. As shown in **Fig. 3** for the lab results, hydraulic fractures crossed the pre-fractures only at high horizontal differential stress and angles of approach of 60° or higher, but hydraulic fractures did not cross the pre-fracture at low horizontal differential stress or low angles of approach. Moreover, hydraulic fractures were arrested by the pre-fracture only at high differential stress and at angles of approach of 30° (Zhou et al. 2008). These results are consistent with Blanton's (1986) and Warpinski and Teufel's (1987) experimental results. Based on the parameters shown in Table 1, PFC was used to numerically model the laboratory hydraulic fracturing tests. Fig. 3 summarizes the modeling results, which can be verified by the resultant cracks and moment tensors of induced seismicity shown in **Figs. 4 through 9** after the fluid injection around 3 seconds. In addition, four more models at different $\Delta\sigma$ and θ were run to testify the crossed and dilated tendency lines shown in Fig. 3 reported by Zhou et al. (2008). Also, it seems that the horizontal principal stresses with a ratio more than 2 may be enough to cross a natural fracture with a single hydraulic fracture.

By virtue of the modeling, we can examine in detail the propagation of cracks outside and within the pre-fractures and the evolution of induced seismicity and its mechanism. In Fig. 4, at $\Delta\sigma$=10MPa the induced fractures were clearly arrested by the pre-fracture and higher fluid pressure was accumulated in front of the pre-fracture, what's more, lots of shear cracks were produced along the pre-fracture. Compared to the moment tensors in Fig. 7, **Fig. 10** shows only shear events and corresponding moment tensors after the fluid injection about 4 seconds. At the interaction between pre-fracture and hydraulic fractures, shear events were triggered along the pre-fracture, which confirms that the arrestment was caused by the shear slippage of the pre-fracture and the shear slippage is the mechanical reason resulting in the much lower fluid pressure within the pre-fracutre. Interestingly, Fig.10 also illustrats that shear events were accompanying with the propagation of hydraulic fractures.

For $\Delta\sigma$ =5MPa at $\theta = 30^\circ$, the pre-fracture was opened by the large tensile force at the interaction between the pre-fracture and induced fracture shown in Fig. 7, and the high fluid pressure dominated a much larger region than the case of the arrestment, which may result from the increasing leakoff into the pre-fracture as mentioned by Warpinski (1991). Moreover, the hydraulic fracture was arrested temporarily by opening and dilating the pre-fracture, which complies with the interaction criterion described by Potluri et al. (2005). Similarly, for $\Delta\sigma$ =7MPa at $\theta = 30^\circ$ in Fig. 4 and $\Delta\sigma$ =3MPa at $\theta = 60^\circ$ in Fig. 5, the hydraulic fractures were momentarily arrested by opening and dilating the pre-fracture as indicated by fluid flow along the pre-fracture. In the case of crossing, the pre-fracture can be easily broken with a single hydraulic fracture at $\Delta\sigma$ =10MPa and $\theta = 90^\circ$, and hydraulic fractures can break out of the pre-fracture with some offsets when $\Delta\sigma$ =10MPa, 7MPa and 5MPa at $\theta = 60^\circ$, what's more, multiple fractures can be induced and fractures seem to propagate through the tip of the pre-fracture. These three modeled crossing types are also consistent with the analysis by Potluri et al. (2005). In addition, the higher for $\Delta\sigma$, the less for multiple strands or segments forming induced fractures. Furthermore, the moment tensors shown in all cases reveal that the hydraulic fractures are opened subparallel to the minimum horizontal principal stress outside the pre-fracture and sub-perpendicular to the pre-fracture within the pre-fracture, at the same time, the forces capable to cross the pre-fracture are generally much smaller than those cracking particles outside the pre-fracture except for the arrestment case. As a whole, the interactions between the pre-fracture and hydraulic fractures are well captured by the PFC models, and the model results provide more detailed information. Additionally, the dilated and crossed tendency lines described by Zhou et al. (2008) may need to be adjusted according the modeling results and the possible region of arrested behavior will be decreased.

Model Validation by Field Treatment Data

As shown in the laboratory and corresponding modeling results, natural fractures can have significant impact on fracture growth. This influence is more complex in the field because natural fractures or faults are ubiquitous. Water-fracs and hybrid-fracs are common stimulation method used in many low-permeability reservoirs. During hydraulic fracturing low-permeability gas reservoirs, microseismic imaging is a predominant method used to measure overall fracture growth (in length, height and azimuth) in real time. Here, the paper is based on the data sets of the Bonner stimulation in the Dowdy Ranch field, East Texas. These treatments involve creating fractues by use of slick water rather than cross-linked gels. Sharma et al. (2004) described detailed information about core and log data collected, fracture treatment stages and fracture diagnostics. **Fig. 11** shows the microseismic data for the Bonner stimulation. Owing to the pre-existing fault, the fracture growth was asymmetrical and arrested in the Bonner layer, but the Bonner treatment was observed to have communicated upward into the Moore and Bossier Marker sands through a fault (Sharma et al. 2004), resulting in a significant amount of out-of-zone fracture height growth. Furthermore, propped or effective fracture half-length derived from pressure buildup analysis and history matching production data were significantly shorter than the created fracture half-length deduced from microseismic locations.

According to the similar procedure to the previous laboratory hydraulic fracturing model, the bonded-particle model was created by use of PFC to simulate a 2D slice of the Bonner reservoir approximately 3974m below the surface. The 500m×500m model was made up of 13,880 particles with an average diameter of 4m, which is significantly larger than the actual grain size because of the high calculation costs. Each particle was therefore assumed to be a large block of sandstone. In the model, the contacts between the blocks were assumed to be joints and a pre-existing fault was also built to capture the heterogeneity of Bonner sand as more as possible. The related parameters and calibration results are shown in Table 2. Note that effective stress is assumed so that the applied stresses (σ_1 and σ_3) equal the actual in-situ stresses minus the pore fluid pressure. Because we did not have the information about the unconfined compressive strength and tensile strength of the core sample, the tensile strength was calculated by use of the method described by Eaton (1975) when we estimated in-situ stresses and pore pressures assuming the overburden pressure gradient 22.6KPa/m (1psi/ft). In addition, estimated from the microseismic mapping result shown in Fig. 11, the pre-existing fault was created with $\theta = 60^\circ$, L_d=~50m, L_h=~43m, L_t=~5.7m, α =0.5 and β =4. Here, the tensile strength was selected one of matching parameters by the PFC model. Unfortunately, it is difficult to match compressive and tensile strengths using PFC at this time possibly due to the round particles. Possible solutions involve creating clusters of particles or using very high resolution models (Potyondy and Cundall 2004). It was thought that it was more important to calibrate the model with the rock tensile strength because hydrofracturing is predominantly a tensile process. Therefore, the modeled compressive strength shown in Table 2 should be lower than the actual value.

Fig.12 shows the total induced microseismicity (MS), cracks, and fluid flow about 3-hour fluid injection in the model. **Fig.13** shows seperately MS and corresponding moment tensors for shear and tensile events. Table 3 lists the hydraulic fracturing main results from the field and model. Compared to Fig.11b, Fig.12 illustrates that the PFC model produces the scope and orientation of induced MS similar to results obtained from the actual recorded MS, and the moment magnitudes are within an order of magnitude of the actual events recorded at Bonner indicating that realistic amounts of energy were being released by the modeled events. The tensile events dominated the propagation of hydraulic fracturing and the shear events only account for about 25% of total induced MS. However, there were generally not enough events in the test to look at the statistics of the magnitude distributions. The reasons for few modeled MS are that on the one hand the current model has a very low resolution, on the other hand once a bond is broken, no more cracking or seismicity will be recorded at that contact. The lower fluid pressure shown in Table 3 may be resulted from the lower compressive strength and coarse resolution for the current model.

Nevertheless, interestingly, a certain amount of MS seems to propagate out of plane through the upper side of the fault due to the opening of the fault. As a result, the hydraulic fractures were arrested by the fault. To illustrate, as shown in **Fig.14**, examined further by the resultant moment tensor the significant tensile event includes many tensile and shear cracks within and outside the fault resulting in the dilation of the pre-fracture, and therefore the leakage of injection fluid shown in Fig.12. Furthermore, the induced cracks appeared to be ahead of the fluid front and that together with the fluid leakoff imply that effective or propped half-length is shorter than the created fracture half-length deduced from microseismic locations, which is the case during the multistage fracturing treatment in the Bossier formation. In addition, the interaction between hydraulic and natural fracntures is also standing within the possible dilated tendency as shown in Fig.3. In conclusion, these matches give confidence that the model is behaving in a realistic way and that levels of deformation and associated energy release are similar in the model and in the field. Because of the 2D nature of the model, the model can only qualitatively capture the process of the propagation of the out-of-zone seismicity recorded in the field. If a 3D model was run realistically, a direct measurement of fracture volume and fluid leakoff calculation would be easily realized.

Conclusions

In the paper, based on the tri-axial fracturing lab experiments presented in other publications and fluid stimulation in the field, with fully dynamic and hydromechanical coupling a 2D discrete element model was successfully validated to simulate fluid stimulation on a reservoir containing a natural fracture by comparing modeling geometries of hydraulic fractures and induced seismicity with actual results in laboratory and field data.

At the lab scale, the PFC^{2D} models simulated a series of fracturing experiments on rock blocks with pre-fractures with different orientation. Promisingly, the model highly captured three interaction types between induced fractures and pre-fractures such as crossing, dilating, and arresting, at the same time, calibrated the dilated and crossed tendency lines with more modeled hydrofracturing tests. Depending on the differential stresses and orientations of pre-fractures the model also domonstrated three types of crossing represented by a single hydrofracture, multiple fractures, and offset fractures. Furthermore, through the seismic mechanism analysis, the models confirmed that the arrestment can be caused by the shear slippage of the pre-fracture and the shear slippage is the mechanical reason resulting in the much lower fluid pressure within the pre-fracutre, what's more, the hydraulic fracture can also be arrested temporarily by opening and dilating the pre-fracture, which may result in the increasing leakoff into the pre-fracture. In addition, the higher for $\Delta\sigma$, the less for multiple strands or segments forming induced fractures. From the modeling results, it was concluded that the horizontal principal stresses with a ratio no less than 2 may be enough to cross a natural fracture with a single hydraulic fracture.

In the field scale, the calibrated model simulated the stimulation conducted in the tight gas reservoir at Dowdy Ranch field. Although the prameters of the fault were assumed, the model produced the scope and orientation of induced fractures similar to results obtained from the actual recorded microseismicity, and a similar seismic magnitude range. Moreover, the model showed deformation and cracking occurring ahead of the fluid pressure front and hydraulic fractures were arrested by the dilation of the fault. At the same time, the leakage of large fluid volume through the fault area was qualitatively prediected by the 2D model. This confirmed that the propped half-length is shorter than the created fracture half-length deduced from microseismic locations, which is the case during the multistage fracturing treatment in the Bossier formation. Therefore, the model is valid and effective and can help examine in detail the micromechanism behind the failure, and the relationship between the induced seismicity and the fluid front through direct observation of the model.

Admittedly, the model is still a gross simplification of the actual situation. In particular, the 2D nature of the models, the low resolution, and the shortage of actual parameters limit the possible quantitative comparisons with actual data. However, the model can still provide some interesting quantitative and qualitative insights into the mechanics behind the interaction between hydraulic and natural fractures in the laboratory and field scales. These types of models could also be used to assist in the design of future injection operations. If the model is assumed to provide a realistic representation of the reservoir, then it could be used to test the effect of altering various parameters (e.g., in-situ stresses, angle of approach, pumping rate, fluid visocosity, natual fracture geometry, etc.). The models could therefore provide a useful tool for optimizing the operations for maximum fracture volume/effective fracture half-length, etc.

Acknowledgement
The authors would like to acknowledge Applied Seismology Consultants Ltd. and the Halliburton Company for providing the hydraulic fracturing datasets. We would also like to thank Dr. Jim Hazzzrd for providing the basic PFC^{2D} fluid functions.

Nomenclature
A = pipe cross-sectional area, mm^2 [m^2]
k = permeability, md
q = flow rate, m/s
q_i = flow injection rate, m^3/s
q_p = flow rate in a pipe, m/s
r = average grain radius, mm [m]
r_g = grain size ratio
w = pipe aperture, mm [m]
w_0 = pipe residual aperture, mm [m]
E = Young's modulus, GPa
F = compressive normal force, N
F_0 = normal force at which the pipe aperture decreases to $w_0/2$, N
L = pipe length, mm [m]
L_d = distance between the wellbore and the center of pre-fracture, mm [m]
L_h = half-length of pre-fracture, mm [m]
L_t = thickness of pre-fracture, mm [m]
K_f = fluid bulk modulus, GPa
Q = rate of volumetric flow, m^3/s
V = volume, mm^3 [m^3]
V_d = volume of a domain, mm^3 [m^3]
V_p = volume of a pipe, mm^3 [m^3]
α = strength ratio
β = residual aperture ratio
θ = angle of approach, degree
μ = fluid viscosity, Pa·s
ν = Poisson's ratio
σ_1 = minimum horizontal stress, MPa
σ_3 = maximum horizontal stress, MPa
σ_c = unconfined compressive strength, MPa
σ_n = normal stress, MPa
σ_t = tensile strength, MPa
τ = shear stress, MPa
ϕ = porosity, %
Δt = time step for fluid calculation, s
ΔP = fluid pressure change within a domain, MPa
ΔV_d = volume change of a domain in one time step, mm^3 [m^3]
$\Delta\sigma$ = horizontal differential stress, MPa

References

Adachi, J., Siebrits, E., Peirce, A., and Desroches, J. 2007. Computer simulation of hydraulic fractures. *Int. J. Rock Mech. Min. Sci.* **44**(5): 739–757. DOI:10.1016/j.ijrmms.2006.11.006.

Akulich, A. V. and Zvyagin, A. V. 2008. Interaction between hydraulic and natural fractures. *Fluid dynamics* **43**(3): 428–435. DOI: 10.1134/S0015462808030101.

Al-Busaidi, A., Hazzard, J. F., and Young, R. P. 2005. Distinct element modeling of hydraulically fractured Lac du Bonnet granite. *Journal of Geophysical Research* **110**, B06302. DOI:10.1029/2004JB003297

Azeemuddin, M., Ghori, S. G., Saner, S., and Khan, M. N. 2002. Injection-induced hydraulic fracturing in a naturally fractured carbonate reservoir: a case study from Saudi Arabia. Paper SPE 73784 presented at the SPE international symposium & exhibition on formation damage control, Lafayette, Los Angeles, 20–21 February.

Bear, J. 1972. *Dynamics of fluids in porous media*. New York: American Elsevier Publishing Company, Inc.

Beugelsdijk, L. J. L., de Pater, C. J., Sato, K. 2000. Experimental hydraulic fracture propagation in multi-fractured medium. Paper SPE 59419 presented at the SPE Asia Pacific conference on integrated modeling for asset management, Yokohoma, Japan, 25–26 April.

Blanton, T. L. 1986. Propagation of hydraulically and dynamically induced fractures in naturally fractured reservoirs. Paper SPE 15261 presented at the SPE/DOE unconventional gas technology symposium, Louisville, Kentuchy, 18–21May.

Britt, L. K. and Hager, C. J. 1994. Hydraulic fracturing in a naturally fractured reservoir. Paper SPE 28717 presented at the SPE international petroleum conference and exhibition, Veracruz, Mexico, 10–13 October.

Cai, M., Kaiser, P. K., Morioka, H., Minami, M., Maejima, T., Tasaka, Y., and Kurose, H. 2007. FLAC/PFC coupled numerical simulation of AE in large-scale underground excavations. *Int. J. Rock Mech. Min. Sci.* **44**(4): 550–564. DOI:10.1016/j.ijrmms.2006.09.013.

Cundall, P. 2000. *Fluid formulation for PFC2D*. Minneapolis, Minnesota, Itasca Consulting Group.

Dong, C. Y. and de Pater, C. J. 2001. Numerical implementation of displacement discontinuity method and its application in hydraulic fracturing. *Comput. Methods Appl. Mech. Engrg.* **191**(8-10):745–760.

Eaton, B. A. 1975. The equation for geopressure prediction from well logs. Paper SPE 5544 presented at the Fall Meeting of the SPE of AIME, Dallas, Texas, 28 September–1 October.

Economides, M. J. and Nolte, K. G. 1989. *Reservoir stimulation*, second edition. New Jersey: Prentice Hall.

Feignier, B. and Young, R. P. 1992. Moment tensor inversion of induced microseismic events–evidence of nonshear failures in the -4<M<-2 moment magnitude range. *Geophys. Res. Lett.* **19**(14): 1503–1506.

Fischer, T., Hainzl, S., Eisner, L., Shapiro, S. A., and Le Calvez, J. 2008. Microseismic signatures of hydraulic fracture growth in sediment formations: observations and modeling. *J. Geophys. Res.* **113**, B02307. DOI:1029/2007JB005070.

Hazzard, J. F., Young, R.P., and Maxwell, S.C. 2000. Micromechanical modeling of cracking and failure in brittle rocks. *J. Geophys. Res.* **105**(B7): 16683-16697.

Hazzard, J. F. and R. P. 2002a. Moment tensors and micromechanical models. *Tectonophysics* **356**(1-3)**:** 181–197.

Hazzard, J. F., Young, R. P., and Oates, S. J. 2002b. Numerical modelling of seismicity induced by fluid injection in a fractured reservoir. *Proc.*, Fifth North American Rock Mechanics Symposium, Toronto, Canada, 1023–1030.

Hazzard, J. F. and Young, R. P. 2004a. Dynamic modelling of induced seismicity. *Int. J. Rock Mech. Min. Sci.* **41**(8): 1365–1376. DOI: 10.1016/j.ijrmms.2004.09.005.

Hazzard, J. F. and Young, R. P. 2004b. Numerical investigation of induced cracking and seismic velocity changes in brittle rock. *Geophys. Res. Lett.* **31**(1), L01604. DOI:10.1029/2003GL019190.

Holt, R. M., Brandshoug, T., and Cundall, P. A. 2000. Discrete particle and laboratory modeling of core mechanics. *Proc.*, Fourth North American Rock Mechanics Symposium, Rotterdam, Balkema, 1217– 1224.

Jaege, J. C., Cook, N. G. W., and Zimmerman, R. W. 2007. *Fundamentals of rock mechanics*. Oxford: Blackwell.

Jing, L., Ma, Y., and Fang, Z. 2001. Modeling of fluid flow and solid deformation for fractured rocks with discontinuous deformation analysis (DDA) method. *Int. J. Rock Mech. Min. Sci.* **38**(3): 343–355.

Le Calvez, J. H., Tanner, K. V., Glenn, S., Kaufman, P., Sarver, D. S., Bennettt, L., Panse, R., and Palacio, J. C. 2006. Using induced microseismicity to monitor hydraulic fracture treatment: a tool to improve completion techniques and reservoir management. Paper SPE 104570 presented at the SPE Eastern Regional Meeting, Canton, Ohio, 11-13 October.

Li, Liming and Holt, R. M. 2002. Simulating stress-dependent permeability of granular media with a fluid-coupled particle model, in L. Li, Ed. Trondheim, eds., *Particle Scale Reservoir Mechanics*, 1-30.

Maxwell, S. and Urbancic, T. 2001. The role of passive microseismic monitoring in the instrumented oil field. *The Leading Edge* **20**(6): 636–639. DOI:10.1190/1.1439012.

Murphy, H. D. and Fehler, M. C. 1986. Hydraulic fracturing of jointed formations. Paper SPE 14088 presented at the SPE international meeting on petroleum engineering, Beijing, 17–20 March.

Norio, T., Yamaguchi, T., and Zyvoloski, G. 2008. The Hijiori Hot Dry Rock test site, Japan Evaluation and optimization of heat extraction from a two-layered reservoir. *Geothermics* **37**(1): 19–52. DOI:10.1016/j.geothermics.2007.11.002.

Pearson, C. 1981. The relationship between microseismicity and high pore pressures during hydraulic stimulation experiments in low permeability granitic rocks. *J. Geophys. Res.* **86**(B9): 7855-7864.

Pine, R. J. and Cundall, P. 1985. Applications of the fluid-rock interaction program (FRIP) to the modelling of hot dry rock geothermal energy systems. *Proc.*, the International Symposium on Fundamentals of Rock Joints, Bjorkliden, Sweden, 293–302.

Potyondy, D. and Autio, J. 2001. Bonded-particle simulations of the in-situ failure test at Olkiluoto. *Proc.*, 38th U.S. Rock Mechanics Symposium, Balkema, The Netherlands, 1553–1560.

Potyondy, D. and Cundall, P. A. 2004. A bonded-particle model for rock. *Int. J. Rock Mech. Min. Sci.* **41**(8): 1329–1364. DOI:10.1016/j.ijrmms.2004.09.011.

Renshaw, C. E. and Pollard, D. D. 1995. An experimentally verified criterion for propagation across unbonded frictional interfaces in brittle, linear elastic materials. *Int. J. Rock Mech. Min. Sci.* **32**(3): 237–249.

Rodgerson, J. L. 2000. Impact of natural fractures in hydraulic fracturing of tight gas sands. Paper SPE 59540 presented at the SPE Permian basin oil and gas recovery conference, Midland, Texas, 21–23 March.

Sasaki, S. 1998. Characteristics of microseismic events induced during hydraulic fracturing experiments at the Hijiori hot dry rock geothermal energy site, Yamagata, Japan. *Tectonophysics* **289**(1-3): 171–188.

Sasaki, S. and Kaieda, H. 2002. Determination of stress state from focal mechanisms of microseismic events induced during hydraulic injection at the Hijiori Hot Dry Rock site. *Pure Appl. Geophys.* **159**(1-3): 489–516.

Sharma, M. M., Gadde, P. B., Sullivan, R., Sigal, R., Fielder, R., Copeland, D., Griffin, L., and Weijers, L. 2004. Slick water and hybrid fracs in the Bossier: some lessons learnt. Paper SPE 89876 presented at the SPE Annual Technical Conference and Exhibition, Houston, Texas, 26–29 September.

Vinod, P. S., Flindt, M. L., Card, R. J., and Mitchell, J. P. 1997. Dynamic fluid-loss studies in low-permeability formations with natural fractures. Paper SPE 37486 presented at the SPE production operations Symposium, Tulsa, 9–11 March.

Warpinski, N. R. 1991. Hydraulic fracturing in tight, fissured media. *J. Pet Tech* **43**(2): 146-152, 208–209. SPE-20154-PA.

Warpinski, N. R. and Teufel, L. W. 1987. Influence of geologic discontinuities on hydraulic fracture propagation. *J. Pet Tech* **39**(2): 209–220. SPE-13224-PA.

Warpinski, N. R., Branagan, P. T., Mahrer, K. D., Wolhart, S. L., and Moschovidis, Z. A. 1999. Microseismic monitoring of the Mounds drill cuttings injection tests. *Proc.*, 37th U.S. Rock Mechanics Symposium, Balkema, Rotterdam, The Netherlands, 1025–1032.

Zhang, X. and Sanderson, D. J. 1996. Numerical modelling of the effects of fault slip on fluid flow around extensional faults. *Journal of Structural Geology* **18**(1): 109–119.

Zhou, J., Chen, M., Jin, Y., and Zhang, G. 2008. Analysis of fracture propagation behavior and fracture geometry using a tri-axial fracturing system in naturally fractured reservoirs. *Int. J. Rock Mech. Min. Sci.* **45**(7): 1143–1152. DOI:10.1016/j.ijrmms.2008.01.001.

Figures

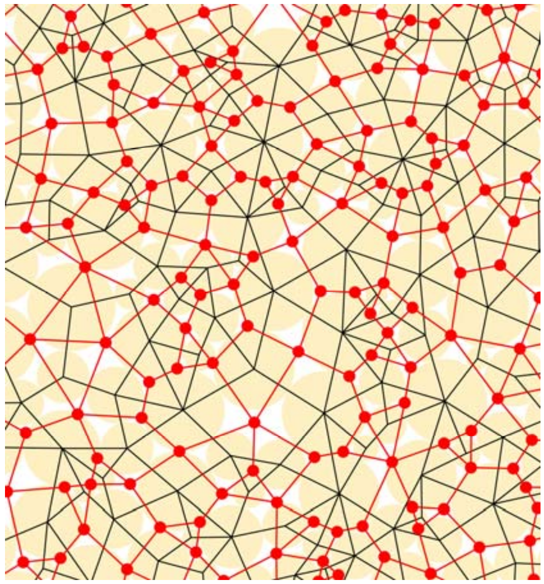

Fig. 1—The fluid network in the PFC model including solid particles (light orange circles), contacts (black lines), flow pipes (red lines) and fluid domains (solid red circles).

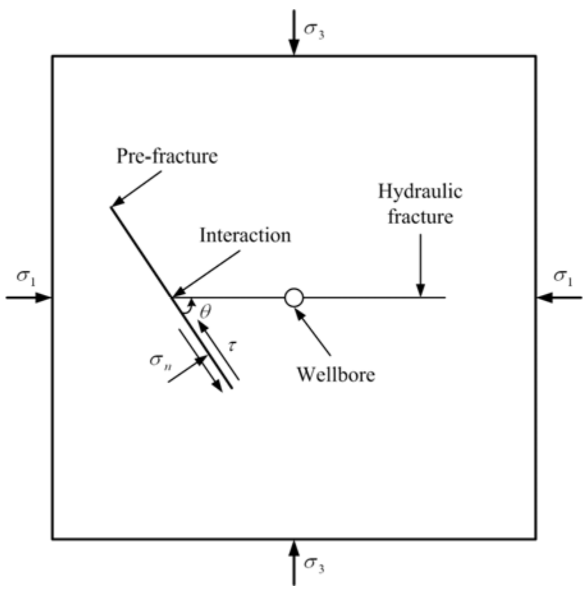

Fig. 2—Schematic view of hydraulic fracture intersecting pre-fracture (modified from Zhou et al. (2008)).

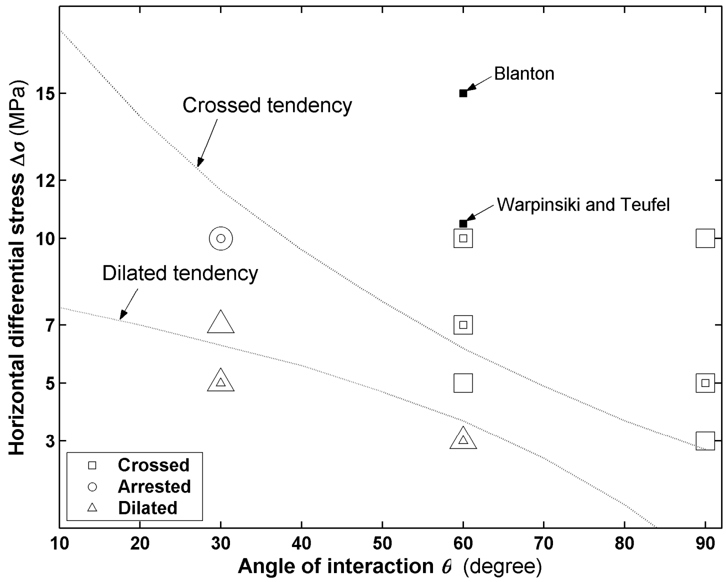

Fig. 3—Laboratory (smaller symbols) (Zhou et al. 2008) and model (larger symbols) results showing the hydraulic fracture behavior for printer paper as the pre-fracture.

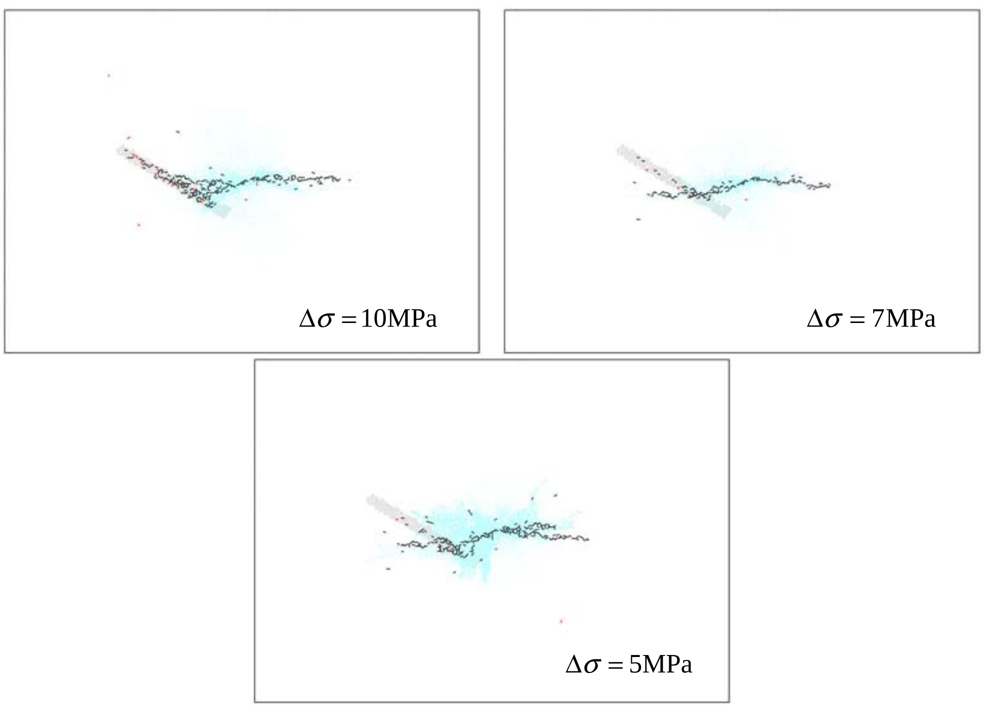

Fig. 4—Indueced cracks (marked by black/red lines corresponding to tensile/shear cracks) and fluid flow (marked by light blue circles whose sizes are scaled to 40MPa) under different $\Delta\sigma$ at $\theta = 30^\circ$ after injecting about 3 seconds. The light gray solid circles are particles within the pre-fractures and the width of the figure is 300mm.

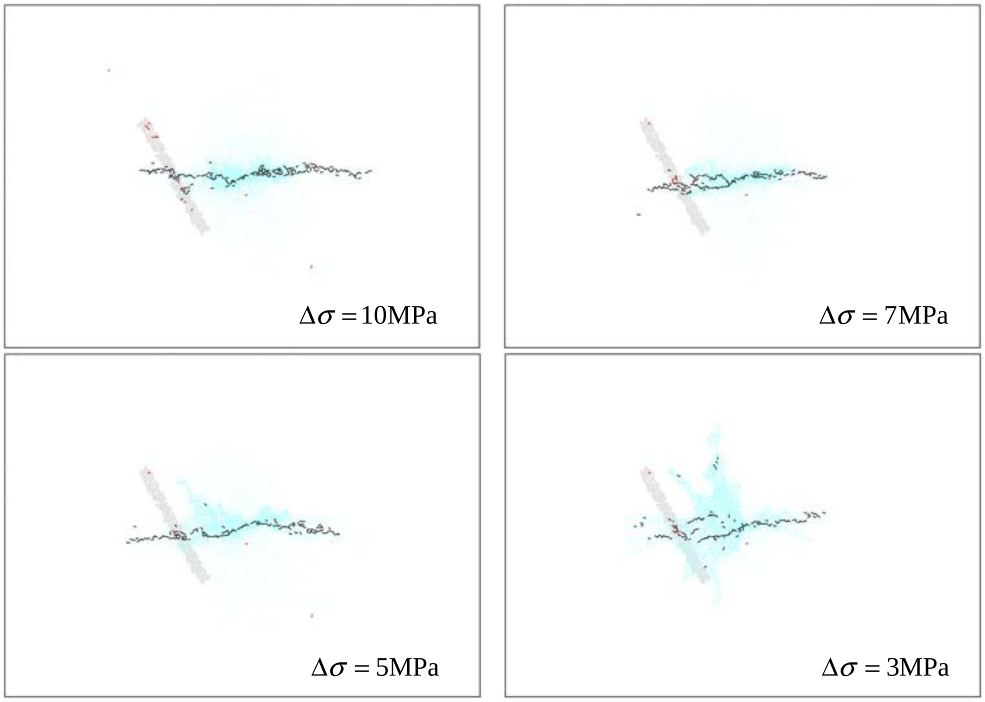

Fig. 5—Indueced cracks under different $\Delta\sigma$ at $\theta = 60^\circ$ after injecting about 3 seconds. The meanings of marks are the same as Figure 4.

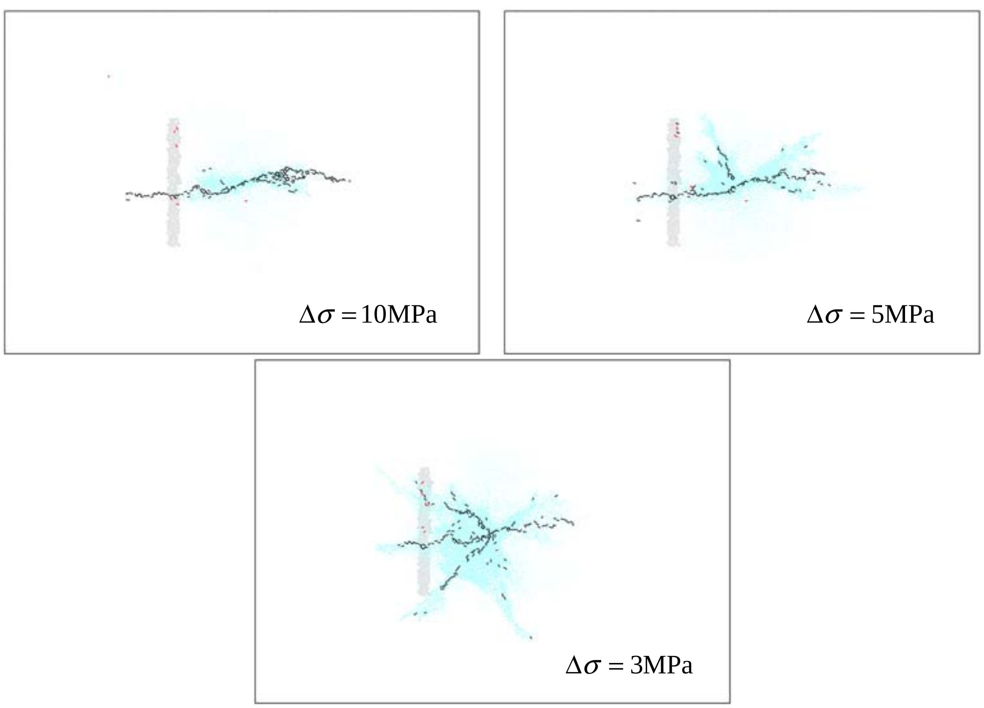

Fig. 6—Indueced cracks under different $\Delta\sigma$ at $\theta = 90^\circ$ after injecting about 3 seconds. The meanings of marks are the same as Figure 4.

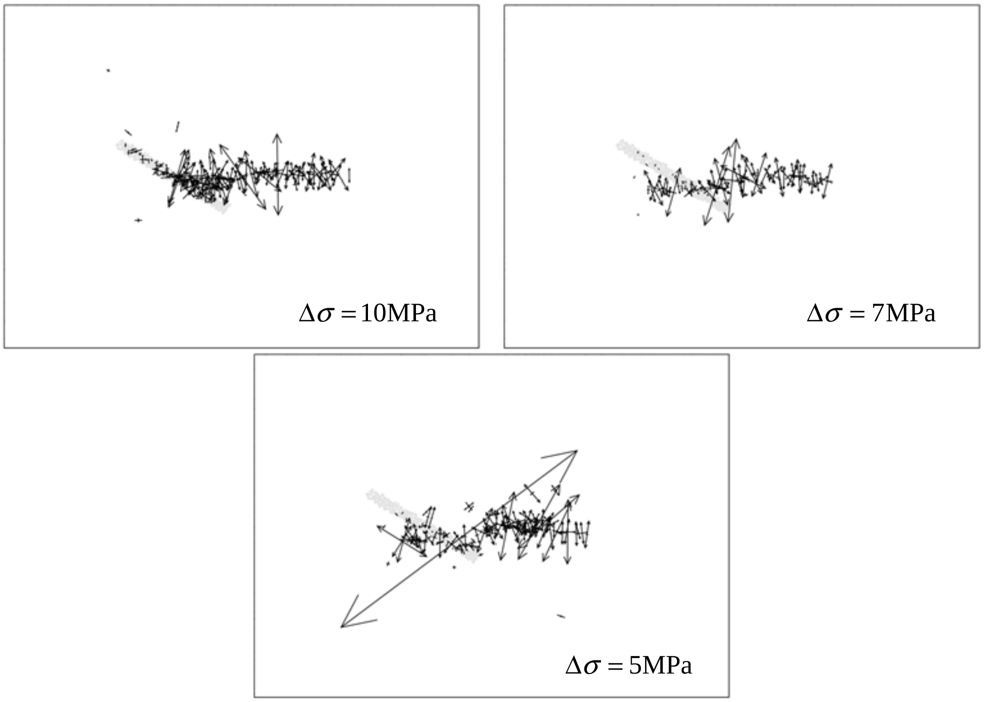

Fig. 7—Moment tensors of induced seismicity under different $\Delta\sigma$ at $\theta = 30^\circ$ after injecting about 3 seconds. The light gray solid circles are particles within the pre-fractures and the width of the figure is 300mm. Note that moment tensors are plotted as equivalent forces, so that two sets of arrows of equal length but opposite polarity represent a perfect double couple (shear) source.

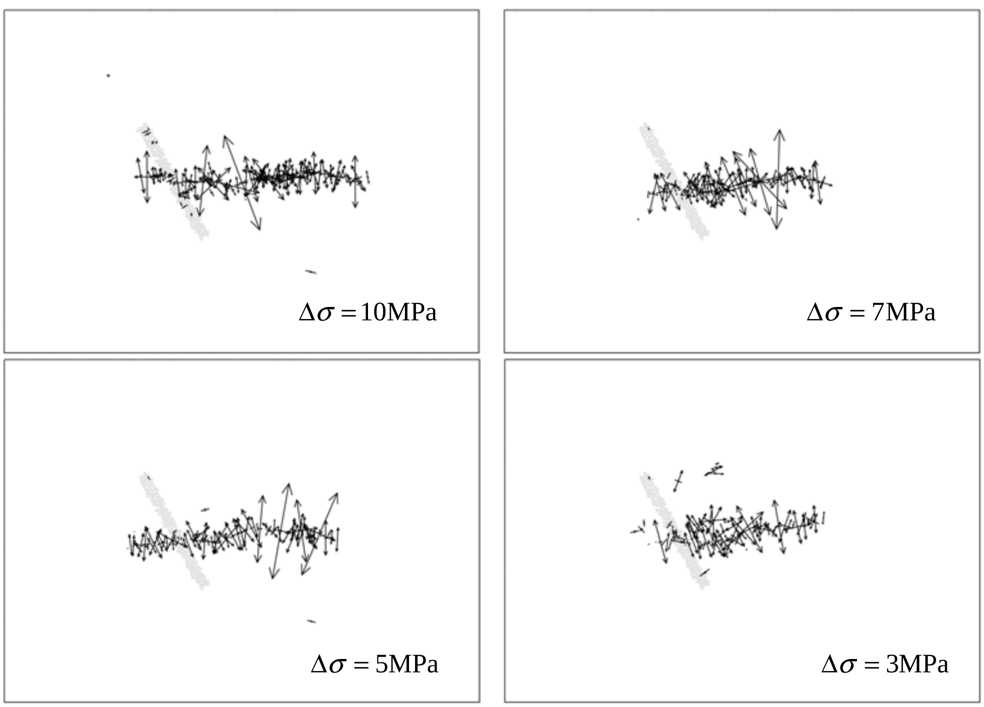

Fig. 8—Moment tensors of induced seismicity under different $\Delta\sigma$ at $\theta = 60^\circ$ after injecting about 3 seconds.

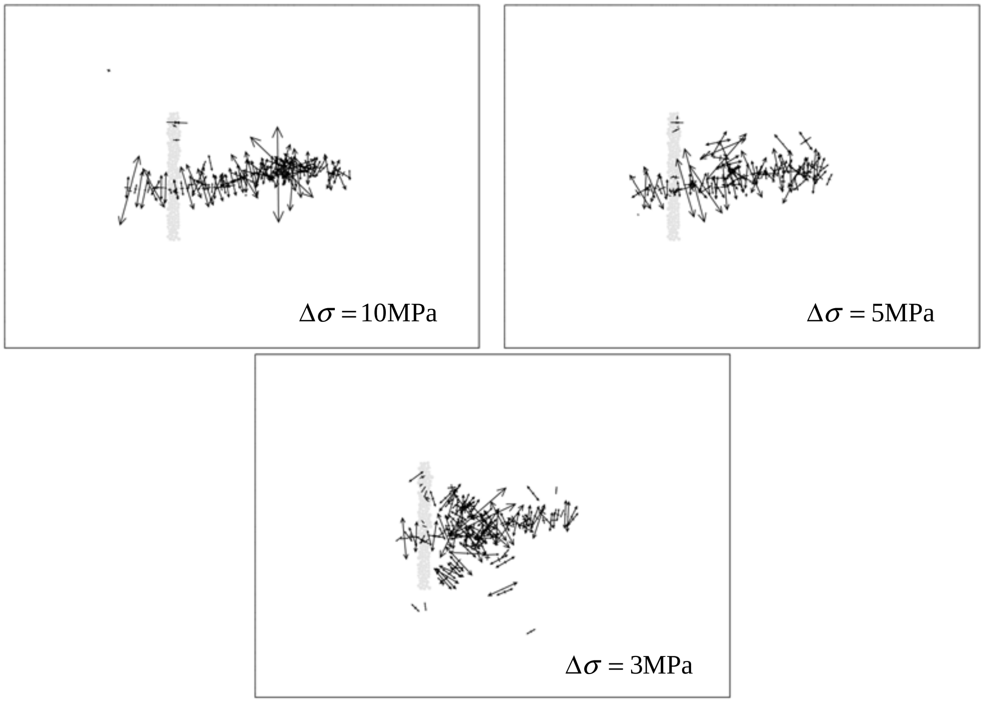

Fig. 9—Moment tensors of induced seismicity under different $\Delta\sigma$ at $\theta = 90^{\circ}$ after injecting about 3 seconds.

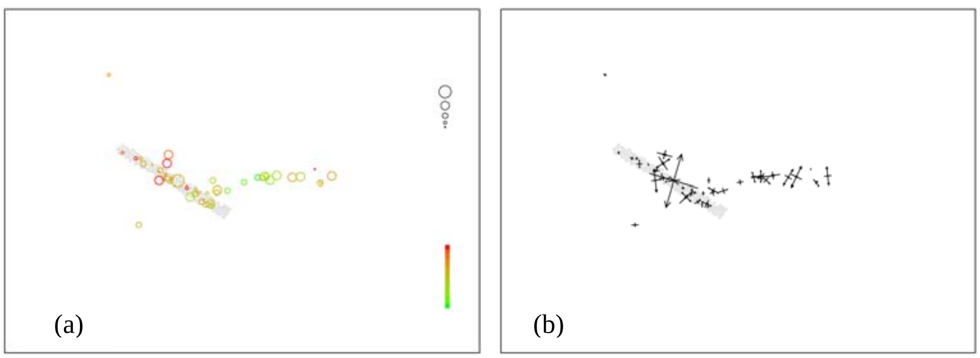

Fig.10—Induced shear seismicity and corresponding moment tensors for $\Delta\sigma$ =10MPa at $\theta = 30^{\circ}$ after injecting about 4 seconds. The width of the figure is 300mm. (a) Seismicity. The sizes of seismic events are scaled according to their magnitude and the color corresponds to the occurring time of seismic events (green/red=early/late). (b) Moment tensors corresponding to (a).

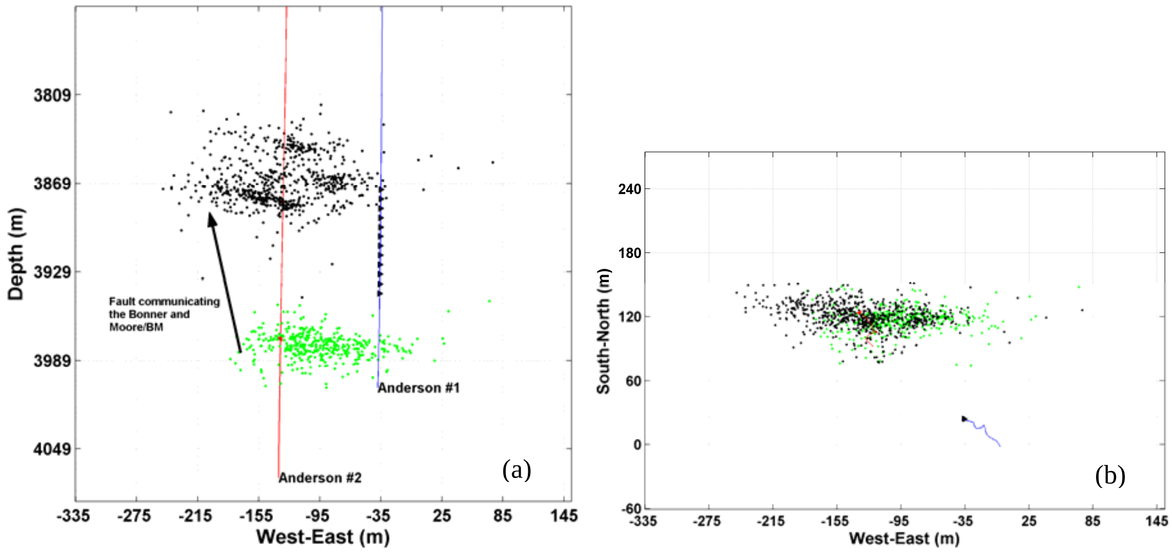

Fig. 11—Microseismic data recorded through the Bonner treatment. The green dots are marked for microseismic events in the Bonner layer and the black dots for microseismic events in the upper layers. The injection well is at Anderson #2 and the monitoring well is at Anderson #1 with a linear receiver array (black triangles). (a) Side view. (b) Plan view.

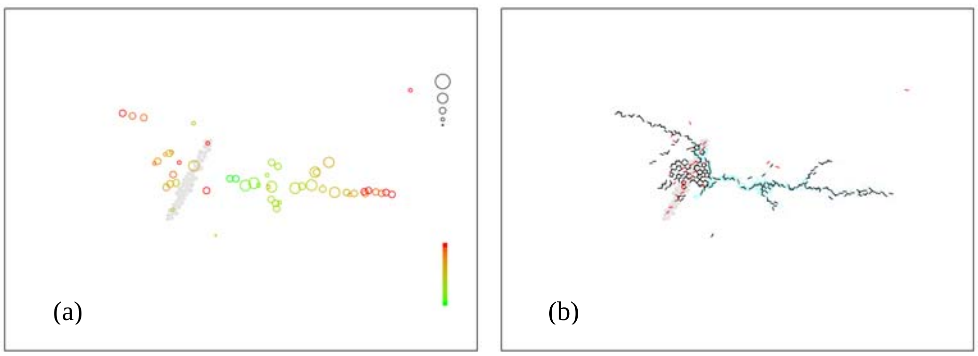

Fig.12—Induced MS and cracks and fluid flow after injecting about 3 hours in the field model. (a) MS. The meanings of colors are the same as Fig.4 and the sizes of circles are scaled to the maximum magnitude of 0.61. (b) Induced cracks and fluid flow. The meanings of marks are the same as Fig.10. The sizes of pressure are scaled to 40MPa.

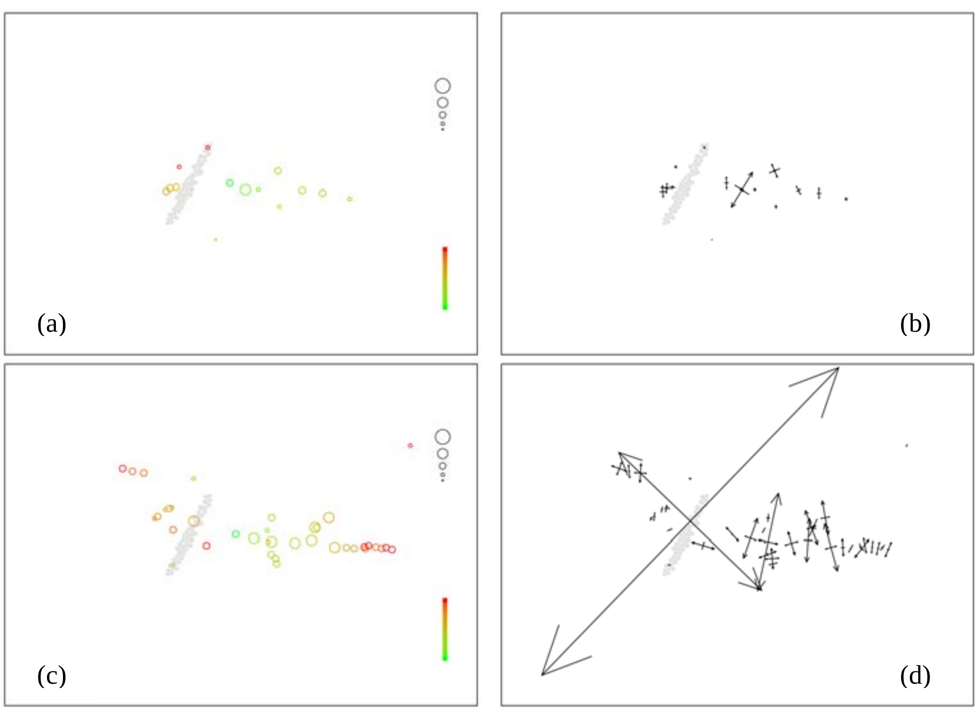

Fig.13—Induced shear/tensile MS and corresponding moment tensors. (a) and (c) Shear and tensile MS. The meanings of marks are the same as Fig.12. (b) and (d) Moment tensors corresponding to (a) and (c), respectively.

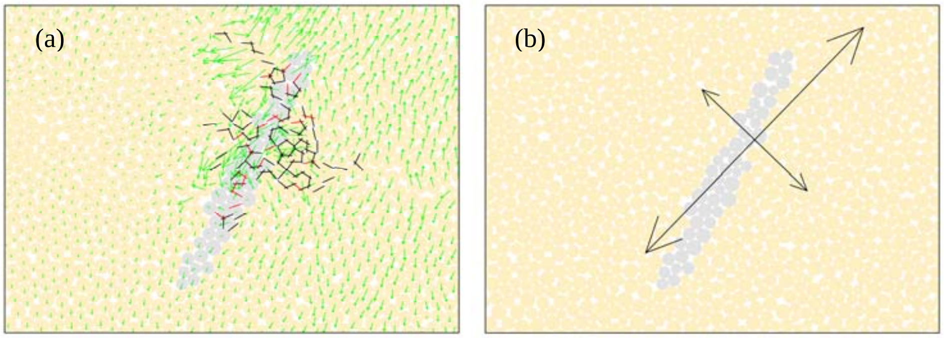

Fig.14—The tensile seismic event composed of 147 cracks corresponding to the larges event shown in Fig.13d. (a) Particle velocities (green arrows) after bond breakages. The crack is represented by a sub-vertical line (black for tensile and red for shear) between the two source particles. (b) The calculated moment tensor. The moment tensor representation depicts the principal values (eigenvalues) of the moment tensor matrix as two sets of arrows whose direction and length indicate the orientation and magnitude, respectively, of the principal values.

Tables

Table 1—Basic parameters for lab hydraulic fracturing tests and PFC model calibration results

Parameters		Laboratory	Model
Sample	r (mm)	~0.09	~0.9
	r_g	2	2
	ϕ (%)	1.85	15.7
	E (GPa)	8.402	8.323
	ν	0.23	0.231
	σ_c (MPa)	28.34	28.49
	σ_t (MPa)	*	6.38
	k (md)	0.1	0.021
Pre-fracture	L_d (mm)	~40	~40
	L_h (mm)	~40	~40
	L_t (mm)	0.11	~5
	α	0.5	0.5
	β	*	2
Fluid	μ (Pa·s)	135×10^{-3}	135×10^{-3}
	K_f (GPa)	10	10
	q_i (m^3/s)	4.2×10^{-9}	1×10^{-6}

*Values are unknown.

Table 2—Basic parameters for Bonner stimulation and PFC model calibration results

Parameters		Actual	Model
Sample	r (m)	$\sim9\times10^{-5}$	~2
	r_g	10	1.66
	ϕ (%)	0.3-11	16
	E (GPa)	44	44.4
	ν	0.22	0.227
	σ_c (MPa)	*	14.8
	σ_t (MPa)	3.24	4.58
	k (md)	0.002-0.1	0.043
Reservoir	σ_1 (MPa)	6.3	6.3
	σ_3 (MPa)	9.6	9.6
Fluid	μ (Pa·s)	1×10^{-3}	1×10^{-3}
	K_f (GPa)	2	2
	q_i (m^3/s)	8.7×10^{-3}	1×10^{-3}

*Values are unknown.

Table 3—Hydraulic fracturing results for the Bonner treatment

Parameters	Field	Model
Number of induced MS	1066 (660/406)[@]	52
Number of shear MS	*	14
Number of explosive/implosive MS	*	31/7
Magnitude range of MS	-0.93~1.15	-1.52~0.61
Fluid pressure (MPa)	<77	<40

*Values are unknown. [@] Number of MS located in the upper/lower (black/green) layer shown in Fig.11.